Acta Materialia 246 (2023) 118673

Contents lists available at ScienceDirect

Acta Materialia

journal homepage: www.elsevier.com/locate/actamat

Full length article

Characterization of gradient plastic deformation in gradient nanotwinned Cu

Zhao Cheng [a,1], Linfeng Bu [a,b,1], Yin Zhang [c], HengAn Wu [b], Ting Zhu [c,*], Lei Lu [a,2,*]

[a] Shenyang National Laboratory for Materials Science, Institute of Metal Research, Chinese Academy of Sciences, Shenyang 110016, China

[b] CAS Key Laboratory of Mechanical Behavior and Design of Materials, Department of Modern Mechanics, CAS Center for Excellence in Complex System Mechanics, University of Science and Technology of China, Hefei 230027, China

[c] Woodruff School of Mechanical Engineering, Georgia Institute of Technology, Atlanta, GA 30332, USA

ARTICLE INFO

Keywords:
Gradient nanotwinned cu
Structural gradient
Distributions of gradient plastic strains
Bundle of concentrated dislocations
Back stress

ABSTRACT

Gradient nanostructured (GNS) metals exhibit high overall extra strengths relative to their non-gradient counterparts. However, the spatial distribution of local extra strengths stemming from plastic strain gradients remains elusive. This work is focused on characterizing the gradient distribution of plastic strains in a representative GNS metal of gradient nanotwinned (GNT) Cu. Full-field strain mapping reveals the gradient distributions of lateral strains in the transverse cross section of GNT Cu samples undergoing uniaxial tensile deformation. We find that the lateral strain gradient increases but the maximum lateral strain difference decreases in GNT samples with increasing structural gradient. The latter arises because the softest layer with the lowest initial yield strength gains the largest local extra strength during tensile deformation, and vice versa. Such a gradient distribution of local extra strengths results from the combined strengthening effects of plastic strain gradient and grain size. These experimental results are used to inform a strain gradient plasticity model for revealing the gradient distributions of local extra back stresses and local extra strengths with increasing load. The coupled experimental and modeling characterization of gradient plastic deformation provides an in-depth mechanistic understanding of the spatial-temporal evolution of gradient strengthening effects in gradient nanostructures.

1. Introduction

Gradient nanostructured (GNS) materials with a spatial distribution of gradient nanostructures can exhibit superior mechanical properties relative to their non-gradient counterparts [1–7]. For example, GNS materials often possess excellent combinations of strength and ductility, whereas these two properties conflict against each other in conventional materials with homogeneous or random microstructures [8]. The gradient plastic deformation across gradient nanostructures needs to be characterized in order to gain a complete understanding of the underlying deformation mechanisms and resultant mechanics effects of GNS materials [9–13]. For example, a distribution of gradient microstructure lengths such as twin thicknesses and grain sizes through the thickness of a GNS sample can lead to a distribution of gradient yield strengths [14]. Under tensile loading, progressive yielding occurs through the sample thickness [15,16], as plastic straining begins in the softest regions with the lowest initial yield strength and extends to the harder ones with increasing load. As a result, the gradient distributions of both elastic and plastic strains develop through the sample thickness [17–19], while the total tensile strain remains nearly uniform. To accommodate the gradients of plastic strain, geometrically necessary dislocations (GNDs) are produced [9], leading to the extra strengthening effects of GNS materials which can be evaluated by gradient plasticity models [10,20–24].

The overall strain of a GNS sample can be readily measured. However, the direct measurement of spatially varying plastic strains remains challenging [25]. The evolution of lateral strains through the sample thickness of GNS materials contains information on gradient plastic strains and has been characterized by means of full-field strain measurements [17,26–28]. For example, the measured lateral strain increases from the soft to hard regions in gradient nanograined (GNG) IF

* Corresponding authors.
E-mail addresses: ting.zhu@me.gatech.edu (T. Zhu), llu@imr.ac.cn (L. Lu).

[1] These authors contributed equally to this work.

[2] Lei Lu was an Editor of the journal during the review period of the article. To avoid a conflict of interest, Lei Lu was blinded to the record and another editor processed this manuscript.

https://doi.org/10.1016/j.actamat.2023.118673
Received 7 November 2022; Received in revised form 17 December 2022; Accepted 2 January 2023
Available online 3 January 2023
1359-6454/

steel [17] and TWIP steel [26], suggesting the distributions of gradient plastic strains.

Recently, gradient nanotwinned (GNT) Cu with dual gradients in twin thickness and grain size has been shown as a favorable GNS system with highly controllable microstructural gradients for studying gradient-dependent mechanical behavior [29–31]. Both the measured strength and work hardening rate of GNT Cu surpass the estimates based on the rule of mixtures using the corresponding values of homogeneous components, while the extra strength and work hardening rate increase with increasing structural gradient. When the structural gradient is sufficiently large, the strength of GNT Cu even exceeds that of the strongest homogeneous component with the finest twin thickness, exhibiting a substantial extra strengthening effect.

The mechanics of the GNS materials has been studied by computational modeling based on non-gradient plasticity models. The gradient plastic strains in GNG Cu were revealed by a crystal plasticity finite element model that accounts for the grain size dependence of yield strength and strain hardening rate [15,32]. Based on the simulated height profile on the side surface of the GNG IF steel samples, a simple physical law was proposed to relate the extra strain hardening and non-uniform deformation [18,33]. Taking deformation twinning into account, a dislocation-based crystal plasticity finite element model was developed to predict the tensile response and lateral contraction of GNS TWIP steel with three gradient microstructures, i.e., gradient grain size, dislocation density and twin fraction [34].

Recently, a strain gradient plasticity (SGP) theory was developed by extending the classical rate-dependent J_2 flow theory and incorporating the strengthening effect of plastic strain gradient into the plastic resistance [35]. The associated numerical simulations revealed several primary characteristics of gradient plasticity in GNT Cu under uniaxial tension, including progressive yielding, gradient distributions of plastic strains and extra plastic resistances. An extended SGP theory was developed to account for the contributions of experimentally measured effective stresses and back stresses to the plastic resistance [36]. Experimental measurements and numerical simulations based on the extended SGP theory showed that the extra strength in GNT Cu relative to non-gradient counterparts is caused predominantly by the extra back stress resulting from nanotwin thickness gradient, while the effective stress is almost independent of structural gradient. Furthermore, an increase of structural gradient in GNT Cu gives rise to an increased plastic strain gradient, thereby raising the extra back stress. Whereas this study has established the mechanistic connections of structural gradient, plastic strain gradient, extra back stress, and extra strength in GNG Cu, there is a lack of direct experimental information on the spatial distributions of gradient plastic deformation. Hence, our understanding of the strengthening effects of GNS materials has been limited to correlations of the sample-level mechanical responses to the structural gradients. The spatial distribution and evolution of gradient plastic strains in GNS materials as well as their effects on the local and overall extra strengths are not clearly understood yet.

In this work, we apply uniaxial tensile loading to four types of GNT Cu samples with different structural gradients and characterize the spatial distributions of gradient lateral strains through the transverse cross section of these samples using a full-field strain mapping technique. We also measure the overall effective and back stresses for each type of GNT Cu samples. Meanwhile, we improve the extended SGP theory by considering the grain size dependence of the saturated extra back stress. Numerical simulations based on the improved SGP theory are calibrated by matching predictions of the sample-level effective and back stresses in GNT Cu samples to experimental values, and further show the spatial distributions of gradient plastic strains which are consistent with the experimental measurements. These simulations reveal the effects of structural gradient on the distributions of local extra back stresses and local extra strengths, which dictate the overall extra back stress and extra strength in GNT Cu.

2. Experimental and modeling methods

2.1. Sample preparation

By means of direct current electrodeposition, four homogeneous nanotwinned (HNT) layers, referred to as Ⓐ, Ⓑ, Ⓒ and Ⓓ, can be prepared at different electrolyte temperatures 20, 25, 30 and 35 °C, respectively. Each HNT layer contains columnar grains that are embedded with nanoscale twin lamellae preferentially orientated perpendicular to the growth direction. The twin thickness and the corresponding grain size increase from 29 to 72 nm and from 2.5 to 15.8 μm for Ⓐ to Ⓓ, respectively. Using these HNT layers as building components, GNT Cu samples were fabricated with the stacking sequences of ⒶⒷⒸⒹ, ⒶⒷⒸⒹⒹⒸⒷⒶ, 2 × ⒶⒷⒸⒹⒹⒸⒷⒶ and 4 × ⒶⒷⒸⒹⒹⒸⒷⒶ, referred to as GNT-1, GNT-2, GNT-3 and GNT-4, respectively [29]. Each periodic stacking sequence was obtained by a stepwise increase of electrolyte temperature from 20 to 35°C and then a stepwise decrease from 35 to 20°C. From GNT-1 to GNT-4, the average rate of change of electrolyte temperature increases from 0.94 to 7.5°C/hour. Each HNT component was deposited at a current density of 30 mA/cm^2 and by a total time of 4 h. As a result, the four types of GNT samples have the same overall thickness of about 400 μm and the same total thickness of each HNT layer Ⓐ, Ⓑ, Ⓒ and Ⓓ. Hence, these four types of GNT samples contain the same volume fraction of each HNT component (25%). However, the individual thickness of the HNT layers decreases from GNT-1 to GNT-4. The twin thicknesses between adjacent HNT layers exhibit smooth and gradual changes without sharp transition.

2.2. Lateral strain measurement

Dog-shaped flat tensile specimens with a gauge section of 5 mm long and 2 mm wide were cut from as-deposited GNT Cu samples using an electric spark machine. All tensile specimens were mechanically polished to reduce surface roughness. Each tensile specimen was put under an Olympus LEXT OLS4100 confocal laser scanning microscopy (CLSM) with a planar resolution of 120 nm and a height resolution of 10 nm to measure the height of the lateral surface (i.e., the *x*-*y* plane as indicated in Fig. 1a). Then, the tensile specimen was taken to an Instron 5848 tester and was elongated to a strain $\varepsilon = 1\%$ under an applied strain rate of 5×10^{-3} s^{-1}. The tensile strain in the gauge section was monitored by a contactless laser extensometer (MTS LX300). After unloading, the deformed tensile specimen was moved back to CLSM and the height of the lateral surface was measured again. For the CLSM measurement, an in-house-built fixture was used to avoid the tensile specimen tilting.

From the measured distribution of lateral surface heights of each tensile specimen, the average profile of lateral surface heights through the specimen thickness (as a function of *y*) was obtained by calculating the mean value of lateral surface heights along the *x* direction at each fixed *y* position. Then the difference in the average profiles before and after tensile deformation was calculated as ΔH (*y*). Hence, the distribution of the relative lateral strain $\Delta\varepsilon_z^{\mathbf{p}}$ is obtained by [26]

$$\Delta\varepsilon_z^{\mathbf{p}}(y) = \frac{2\Delta H(y)}{W} \tag{1}$$

where W is the width of tensile sample before deformation, and the factor of 2 in Eq. (1) implies the same amount of $\Delta H(y)$ on the back lateral surface as the front lateral surface of the specimen. The position with the smallest absolute value $|\Delta H|$ is offset to zero as the reference point, since we are interested in the relative change of $\Delta H(y)$ for determining the distribution of gradient lateral strains. The difference in the lateral strain between Ⓐ and Ⓓ in every period, $\Delta\varepsilon_z^{\mathrm{p,A-D}}$, is obtained from the height difference according to Eq. (1). The lateral strain gradient $\nabla\varepsilon_z^{\mathbf{p}}$ is estimated by linear fitting of the slope of the $\Delta\varepsilon_z^{\mathrm{p}}(y)$ curve between Ⓐ and Ⓓ in every period. Note that $\Delta\varepsilon_z^{\mathrm{p,A-D}}$ and $\nabla\varepsilon_z^{\mathbf{p}}$

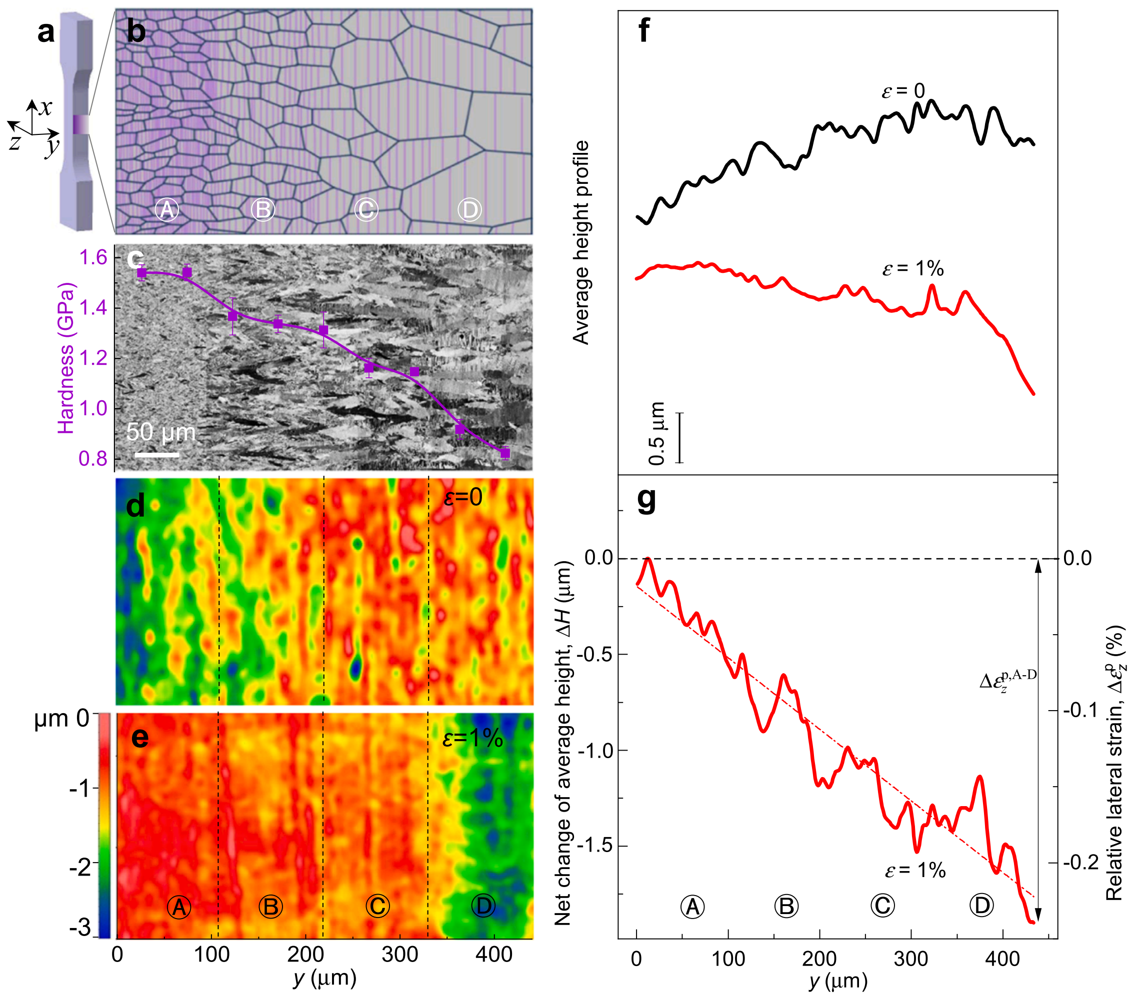

Fig. 1. Distribution of lateral strains in the transverse cross section (x-y plane) of GNT-1. (a) Schematic of a tensile sample where the x, y and z axes are illustrated. (b) Schematic of GNT microstructure through the sample thickness. (c) Corresponding SEM image and hardness distribution. (d) Measured height contour on the lateral surface at $\varepsilon = 0$. (e) Same as (d) except $\varepsilon = 1\%$. (f) Average height profiles through the sample thickness at $\varepsilon = 0$ and 1%, as extracted from (d) and (e), respectively. (g) The net change of average height $|\Delta H|$ at $\varepsilon = 1\%$ relative to that at $\varepsilon = 0$ where the smallest $|\Delta H|$ is set zero as the reference point (left axis), and the corresponding distribution of average relative lateral strain $\Delta\varepsilon_z^{\mathbf{p}}$ (right axis).

characterize the plastic strain distribution from the ex-situ CLSM measurement of an unloaded sample where elastic strains have been fully relaxed. The mean value $\overline{\Delta\varepsilon_z^{p,A-D}}$ and its error are obtained by averaging more than three measured values of $\Delta\varepsilon_z^{p,A-D}$. The same protocols were used to obtain the mean value $\overline{\nabla\varepsilon_z^{\mathbf{p}}}$ and its error bar from measurements of $\nabla\varepsilon_z^{\mathbf{p}}$.

2.3. Microstructure characterization

The cross-sectional microstructures of as-deposited and deformed GNT Cu samples were examined by a scanning electron microscope (SEM, FEI Nova NanoSEM 460) equipped with a circular backscattering (CBS) detector and also by a transmission electron microscope (TEM, FEI Tecnai G2 F20) under an accelerated voltage of 200 kV. The dislocation structures of deformed GNT Cu samples were characterized by means of the dual-beam diffraction technique: under diffraction vectors of $g_M = g_T = 111$, Mode I dislocations in both the matrix and twin lamellae were simultaneously imaged; under diffraction vectors of $g_M = 200$ or $g_T = 200$, Mode II dislocations in either the matrix or twin lamellae were imaged. SEM specimens were electrochemically polished in a solution composed of phosphoric acid (25%), alcohol (25%) and deionized water (50%) at room temperature, and TEM specimens were electrochemically thinned in the same solution at −10 C.

2.4. Strain gradient plasticity modeling

As noted in the Introduction, we recently developed a SGP theory by extending the classical J_2 flow theory of plasticity [35]. In the rate-dependent formulation of the SGP theory, a scalar measure of plastic strain gradients is introduced into a hardening rate relation of the plastic resistance. The numerical results based on the SGP theory agree with the experimental measurements of the sample-level extra strengths arising from plastic strain gradients in GNT Cu. We extended the SGP theory to account for the contributions of effective and back stresses to the plastic resistance [36]. Based on the experimental measurements of the sample-level effective and back stresses in HNT and GNT Cu, a term representing the local extra back stress is introduced to account for the extra strengthening effect of plastic strain gradients. The nonlinear evolution of the local extra back stress with increasing plastic strain is characterized by a rate equation giving the saturated local extra back stress at large plastic strains. Our numerical calculations based on the extended SGP theory can predict the sample-level extra back stresses in GNT Cu with different structural gradients, which match the corresponding experimental measurements. In the extended SGP theory, the saturated local extra back stress is assumed to be independent of both twin thickness and grain size. As a result, a uniform distribution of saturated local extra back stresses is predicted through the cross section of each GNT sample. However, the experimental measurements in the present work show the decreased $\Delta\varepsilon_z^{p,A-D}$ with increasing structural gradient. These results imply a non-uniform distribution of saturated local extra back stresses through the sample cross section, which is at variance with the assumption of the extended SGP theory, i.e., a uniform distribution of saturated local extra back stresses through the cross section of each GNT sample.

To address the above problem, we improve the extended SGP theory by considering the grain size dependence of the saturated local extra back stress. The detailed formulation of the improved SGP theory is described in the Supplementary Information. Here we derive a scaling relation for the grain size dependence of the saturated local extra back stress in GNT Cu. In general, dislocations tend to aggregate to form low-energy heterogeneous structures such as dislocation cells, which comprise the cell walls with high dislocation densities and the cell interiors with low dislocation densities. To accommodate geometrical incompatibilities between the cell walls and cell interiors during plastic deformation, GNDs are usually formed, resulting in long-range, directional internal stresses associated with dislocation cells. The self-equilibrating internal stresses include the forward stresses acting on the cell walls and the back stresses on the cell interiors, the latter of which dictate the sample-level back stress that is experimentally measurable [37–39]. GNT Cu exhibits a unique type of heterogeneous dislocation structure of bundles of concentrated dislocations (BCDs) inside columnar grains. Our recent experimental studies indicate that the GNDs associated with BCDs can be responsible for the generation of extra back stresses in GNT Cu. Consider a grain that has a size d and contains a BCD. Suppose L is the average spacing between neighboring BCDs in different grains, such that there is one BCD in the center of a cluster of grains with the cross-sectional area $L\times L$, as observed from TEM [29,36]. Assuming each BCD contains N GNDs, we estimate the average density of GNDs as

$$\rho_G^{GNT} \sim \frac{N}{L^2} \tag{2}$$

Here ρ_G^{GNT} is related to the local plastic strain gradient $|\nabla\bar{\varepsilon}^p|$ [9] according to $\rho_G^{GNT} \sim |\nabla\bar{\varepsilon}^p|/b$. Supposing N GNDs aggregate around a BCD residing in a grain, we treat these GNDs as a super-dislocation with the Burgers vector length Nb. These GNDs are dislocations of the same sign and they collectively impose a directional, long-range stress/resistance to a mobile dislocation. This resistance is called the back stress arising from the BCD and it is proportional to the number of GNDs, N, which can be estimated by the GND density from Eq. (2). The average distance between mobile dislocations and GNDs is proportional to the grain size d [40]. Hence, this back stress in the grain containing the BCD can be expressed as

$$\sigma_b^{BCD} \sim \frac{\mu N b}{d} \tag{3}$$

where μ is the shear modulus. In fact, only some grains contain BCDs from experimental observations (Section 3.2). Hence, this BCD is shared by $(L/d)\times(L/d)$ grains. The saturated back stress associated with GNT, σ_{sat}^{GNT}, is estimated by mapping the BCD-induced back stress in a grain, σ_b^{BCD} in Eq. (3), to the BCD-induced back stress in the cluster of grains,

$$\sigma_{sat}^{GNT} = \sigma_b^{BCD}\left(\frac{d}{L}\right)^2 \tag{4}$$

Combining Eqs. (2-4), we obtain an estimate of the saturated local extra back stress

$$\sigma_{sat}^{GNT} = \kappa\mu b d \rho_G^{GNT} \tag{5}$$

where κ is a dimensionless parameter. Eq. (5) indicates that the saturated local extra back stress increases linearly with the grain size and GND density. This scaling relation provides a functional form to represent the grain size dependence of the saturated local extra back stress in the improved SGP theory (see the detailed constitutive equations in the Supplementary Information).

To apply the improved SGP theory for numerical simulation of the gradient plastic deformation in GNT Cu under uniaxial tension, we focus on a simplified 1D model with a prescribed distribution of gradient yield strengths through the sample thickness. Since the tensile stress along the loading direction is the only nonzero stress component, the general 3D SGP theory can be reduced to a 1D SGP theory. Correspondingly, the equivalent effective stress $\bar{\sigma}$ is reduced to the tensile effective stress σ^{eff} and the equivalent plastic strain $\bar{\varepsilon}^p$ is reduced to the tensile plastic strain ε_x^p, etc. With such simplifications, the distributions of elastic and plastic strains in both the x and z directions are obtained for GNT-1 to GNT-4 using the same numerical integration procedure as in Ref. [36]. The material parameters used are listed in Table 1.

The experimental characterization of lateral strains in this work provides the crucial spatial information of gradient plastic deformation for improving the SGP theory. Due to the Poisson's effect [41], the distribution of lateral strains in the transverse cross section (x-y plane) can be correlated to the distribution of tensile plastic strains in the normal cross section (y-z plane) along the loading direction. For example, the lateral plastic strain ε_z^p along the sample width (z axis) can be directly related to the tensile plastic strain ε_x^p along the tensile loading direction (x axis) by

$$\varepsilon_z^p = -\nu\varepsilon_x^p \tag{6}$$

where ν is a constant coefficient. For HNT Cu with a strong {111} texture, the lateral plastic strain ε_z^p parallel to twin boundaries (TBs) is much larger (~7 times) than that perpendicular to TBs (ε_y^p) when the loading direction is parallel to TBs [42]. Considering this plastic anisotropy, we assume that $\varepsilon_y^p = 0$ and $\varepsilon_z^p = -\varepsilon_x^p$, such that $\nu = 1$ and plastic incompressibility ($\varepsilon_x^p + \varepsilon_y^p + \varepsilon_z^p = 0$) is satisfied. Such anisotropic plastic deformation mainly originates from the predominant mechanism of gliding of Mode II dislocations along TBs [42]. Hence, such anisotropic plastic deformation enables us to compare ε_x^p from model predictions with ε_z^p from experimental measurements.

To validate the numerical results from the 1D model, we have also performed 3D finite element simulations by implementing the improved SGP theory through writing a user material subroutine VUMAT in ABAQUS/Explicit [35]. The finite element model for each type of GNT Cu is a thin sample of 400 μm × 400 μm × 50 μm, which is meshed with 32 × 32 × 4 eight-node brick elements with full integration (C3D8) (Fig. S4). To simulate uniaxial tension, the boundary conditions are prescribed as follows: the velocity along the x direction is 0.5 nm/s on the front y-z surface, while the displacement in the x direction is fixed on the back y-z surface; the top and bottom x-z surfaces are traction free.

For clarification, Table 2 lists the major symbols used in this work.

Table 1
Parameters used in strain gradient plasticity simulations.

Symbol (unit)	Magnitude
E (GPa)	115
μ (GPa)	42
ν	0.3
m	500
$\dot{\varepsilon}_0^p (s^{-1})$	0.001
M	3.0
α	0.3
b (nm)	0.255
$k_1 (m^{-1})$	5e9
k_2	5e2
k_3	3e5
c^{HNT}	1e4
c^{GNT}	5e2
κ	27

Table 2
Definitions of symbols used in the main text.

Symbol	Definition
ΔH	Difference in the average height profiles before and after deformation
W	Width of tensile sample before deformation
$\Delta\varepsilon_z^p$	Relative lateral strain
$\Delta\varepsilon_z^{p,A-D}$	Difference of $\Delta\varepsilon_z^p$ between component Ⓐ and Ⓓ
$\overline{\Delta\varepsilon_z^{p,A-D}}$	Mean value of $\Delta\varepsilon_z^{p,A-D}$
ε_x^p	Plastic strain in the tensile direction
$\nabla\varepsilon_z^p$	Lateral strain gradient
$\overline{\nabla\varepsilon_z^p}$	Mean value of $\nabla\varepsilon_z^p$
$\nabla\varepsilon_x^p$	Tensile plastic strain gradient
$\overline{\nabla\varepsilon_{ref}^p}$	Average plastic strain gradient without considering the gradient effect
$\Delta\sigma^{A-D}$	Difference in flow stress between component Ⓐ and Ⓓ
σ_b^{GNT}	Local extra back stress
$\overline{\sigma}_b^{GNT}$	Sample-level extra back stress

Note that we use σ and ε to represent the applied sample-level tensile stress and strain, respectively. To study the distributions of local strains in the x-y and y-z sections of a GNT sample, we use the subscripts x and z to explicitly indicate the normal strain components along the x and z directions, respectively. However, considering that only tensile stress components in the y-z section of a GNT sample are non-zero, we drop the subscript x for those normal stress components, including the associated normal effective stress and back stress.

3. Results and discussion

3.1. Gradient distributions of lateral strains from full-field mapping

The microstructures of GNT-1 to GNT-4 samples used in this work are the same as those in our previous studies [29,43,44]. Notably, these GNT samples have dual gradients in grain size and twin thickness, giving an increased gradient of hardness (measured locally by micro-indentation) along the sample thickness direction from GNT-1 to GNT-4. The structural gradient is represented by the increase in hardness per unit length along the sample thickness direction. The corresponding hardness gradient increases from 1.75 GPa/mm of GNT-1 to 11.6 GPa/mm of GNT-4. From our previous tensile tests [29], the measured tensile yield strength of GNT-1 is 364 MPa, which is slightly higher than the rule-of-mixtures mean (347 MPa) of tensile yield strengths of four constituent HNT components; and the measured yield strength of GNT-4 increases to 481 MPa, which exceeds the yield strength of the strongest component Ⓐ (446 MPa).

As an example of our full-field mapping results of lateral strain distributions, Fig. 1a and b show the schematic of a tensile sample GNT-1 and its microstructure in the transverse cross section (x-y plane), respectively. The HNT components Ⓐ, Ⓑ, Ⓒ and Ⓓ are stacked sequentially, yielding a gradual increase in grain size and twin thickness along the sample thickness direction, as shown by the SEM image in Fig. 1c. The hardness decreases linearly from 1.5 to 0.8 GPa from Ⓐ to Ⓓ along the depth with the structural (i.e., hardness) gradient of 1.75 GPa/mm, as shown in Fig. 1c. To characterize the lateral strain distribution, Fig. 1d shows the lateral surface heights of as-prepared GNT-1 (i.e., the applied tensile strain $\varepsilon = 0$), which are uneven with a small, but gradual increase from Ⓐ to Ⓓ. Such unevenness arises likely from mechanical polishing. In contrast, the lateral surface heights decrease markedly from Ⓐ to Ⓓ after tensile deformation at ε=1% (Fig. 1e). Correspondingly, the average profiles of lateral surface heights as a function of depth y at $\varepsilon = 0$ and 1% are displayed in Fig. 1f. The net change of the average height ΔH is obtained by subtracting the average height profile at $\varepsilon = 1\%$ from that at $\varepsilon = 0$. Fig. 1g shows that the absolute value of $|\Delta H|$ increases linearly with depth y and reaches 1.8 μm across the x-y section. This indicates a gradient distribution of lateral strains $|\Delta\varepsilon_z^p(y)|$ according to Eq. (1). The lateral strain difference $|\Delta\varepsilon_z^{p,A-D}|$ is estimated from the data at $y = 60$ and 380 μm, which corresponds to the middle of Ⓐ and Ⓓ, respectively. The average lateral strain difference $|\overline{\Delta\varepsilon_z^{p,A-D}}|$ of GNT-1 reaches 0.19% and the average lateral strain gradient $|\overline{\nabla\varepsilon_z^p}|$ is estimated as 4.8 m^{-1}.

For comparison, the distribution of lateral strains in GNT-3 with a larger structural gradient (6.0 GPa/mm) is shown in Fig. 2. Both the schematic microstructure (Fig. 2a) and the SEM image (Fig. 2b) of GNT-3 show the stacking sequence of 2 × ⒶⒷⒸⒹⒹⒸⒷⒶ with two periods of microstructure variation. Correspondingly, the distribution of indentation hardnesses exhibits two triangular waves with the structural (i.e., hardness) gradient of 6.0 GPa/mm (Fig. 2b). The as-prepared GNT-3 sample has a relatively smooth lateral surface (Fig. 2c), but the height profile on the lateral surface becomes wavy at $\varepsilon = 1\%$ (Fig. 2d). Both the average heights as a function of depth y at $\varepsilon = 0$ and 1% are shown in Fig. 2e and the net change of average height ΔH at $\varepsilon = 1\%$ of is displayed in Fig. 2f. Obviously, ΔH exhibits a dual-triangle wave along the y direction, which is similar to the dual-triangle wave distribution of hardness (Fig. 2b). Like GNT-1, both $|\Delta H|$ and $|\Delta\varepsilon_z^p|$ in GNT-3 exhibit gradient distributions and reach the minimum at Ⓐ and the maximum at Ⓓ. However, the average $|\overline{\Delta\varepsilon_z^{p,A-D}}|$ for GNT-3 at $\varepsilon = 1\%$ is only 0.05%, which is about a quarter of that for GNT-1. The average lateral strain gradient $|\overline{\nabla\varepsilon_z^p}|$ of GNT-3 reaches 5.8 m^{-1}, which is 21% higher than that of GNT-1.

Fig. 3 shows the evolution of $|\overline{\Delta\varepsilon_z^{p,A-D}}|$ (left y axis) and $|\overline{\nabla\varepsilon_z^p}|$ (right y axis) with structural gradient. It is seen that $|\overline{\Delta\varepsilon_z^{p,A-D}}|$ decreases rapidly from 0.19 to 0.04% when the structural gradient increases from 1.75 (GNT-1) to 11.6 GPa/mm (GNT-4). However, $|\overline{\nabla\varepsilon_z^p}|$ shows an opposite trend and increases from 4.8 to 8.2 m^{-1} from GNT-1 to GNT-4. Although the structural gradient increases by a factor of about seven, the lateral strain gradient $|\overline{\nabla\varepsilon_z^p}|$ of GNT-4 is only twice that of GNT-1. This suggests that the increase of the overall plastic strain gradient of GNT Cu is reduced with increasing structural gradient, mainly due to a substantial reduction in $|\overline{\Delta\varepsilon_z^{p,A-D}}|$.

3.2. BCDs and GNDs from TEM characterization

In order to clarify the gradient strain response to structural gradients, we studied the deformation microstructure of GNT Cu by means of TEM diffraction. We found a large amount of BCDs with associated GNDs that can contribute to the extra strengthening of GNT Cu relative to HNT Cu samples without BCDs. Taking GNT-3 at $\varepsilon = 1\%$ as an example, the BCD that is aligned along the structural gradient direction (perpendicular to TBs) and across multiple twin lamellae in component Ⓐ can be easily identified in Fig. 4a. The strong contrast of the BCD results from the significant misorientation (5–8°) caused by GNDs with Burgers vectors of the same sign [21,45,46]. Both SEM and TEM observations indicated that such kind of BCDs structure is present in parts of grains (more than 10%).

A dual-beam diffraction technique is used to characterize the detailed microstructure of BCDs [47]. From the TEM image in Fig. 4b with a diffraction vector of $g_M = g_T = 111$, a few dislocation lines (indicated by green arrows) traversing multiple twin lamellae are clearly seen. These dislocations are identified as Mode I dislocations with both their Burgers vectors and glide planes inclined to TBs. Under the diffraction vector of $g_M = 200$ (Fig. 4c), many dislocation debris (indicated by orange arrows) appear at TBs and these are identified as Mode II dislocations with their Burgers vectors parallel to TBs but glide planes inclined to TBs (Fig. 4c). The density of Mode I dislocations is much lower than that of Mode II dislocations.

With increasing grain size, more BCDs are detected in component Ⓓ, as shown in Fig. 4d. The size (parallel to TBs) of BCDs become wider (~1.5 μm) in Ⓓ relative to Ⓐ (0.3 μm), while the misorientation is comparable in both components. Dual-beam diffraction TEM

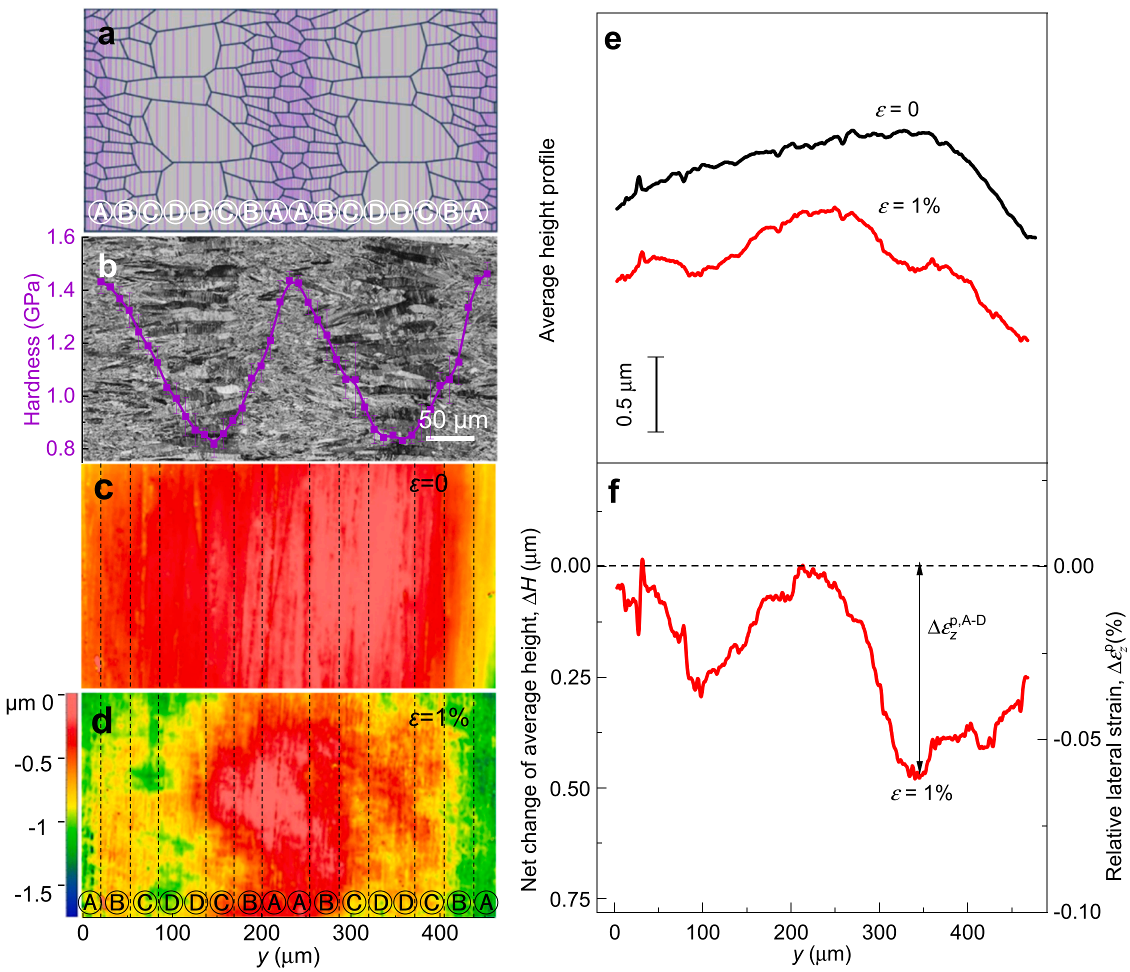

Fig. 2. Distribution of lateral strains in the lateral surface (x-y plane) of GNT-3. (a) Schematic of GNT microstructure through the sample thickness. (b) Corresponding SEM image and hardness distribution. (c) Measured height contour on the lateral surface at $\varepsilon = 0$. (d) Same as (c) except $\varepsilon = 1\%$. (e) Average height profiles through the sample thickness at $\varepsilon = 0$ and 1%, as extracted from (c) and (d), respectively. (f) The net change of average height $|\Delta H|$ at $\varepsilon = 1\%$ relative to that at $\varepsilon = 0$ (left axis) and the corresponding distribution of average relative lateral strain $\Delta\varepsilon_z^{\mathbf{p}}$ (right axis).

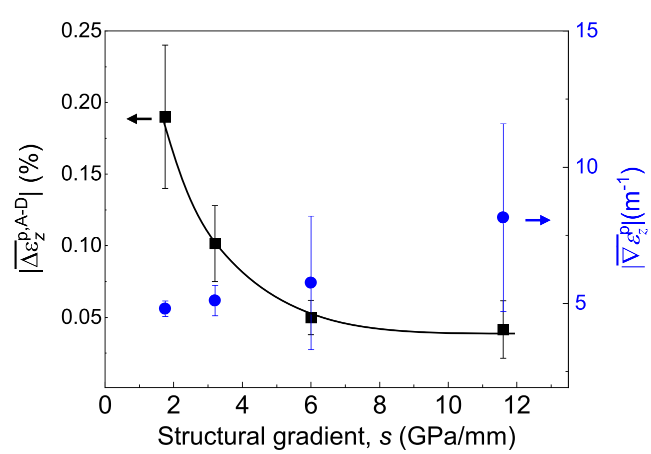

Fig. 3. The average lateral strain difference between components Ⓐ and Ⓓ $|\overline{\Delta\varepsilon_z^{p,A-D}}|$ (left y axis) and lateral strain gradient $|\overline{\nabla\varepsilon_z^{\mathbf{p}}}|$ (right y axis) from GNT-1 to GNT-4.

observations further confirmed that BCDs are formed from a few Mode I (Fig. 4e) and numerous Mode II dislocations (Fig. 4f), similar to those in Ⓐ. Parts of Mode I or Mode II dislocations serve as GNDs to accommodate plastic strain gradients [36,48].

3.3. Gradient distributions of plastic strains from SGP modeling

Our numerical results of GNT models based on the improved SGP theory reveal the effects of structural gradients on the plastic response of GNT Cu. As shown in Fig. S2, both the 1D and 3D GNT models capture the overall stress-strain response and the evolution of the sample-level back stress and effective stress in GNT-1 to GNT-4, all of which are in close agreement with the experimental results [29,36]. Fig. 5a shows the distributions of plastic strains at $\varepsilon = 1\%$ in the normal cross section (y-z plane) of GNT-1 to GNT-4. All four GNT samples exhibit a nearly linear profile of increasing plastic strain from the normalized position $\hat{y} = 0$ to 1, i.e., from Ⓐ to Ⓓ. Interestingly, from GNT-1 to GNT-4, the decrease of plastic strain at $\hat{y} = 0$ is much smaller than that at $\hat{y} = 1$, indicating a reduced lateral strain difference across the sample thickness. Correspondingly, Fig. 5b shows that $\Delta\varepsilon_x^{p,A-D}$ (i.e., the difference in tensile plastic strains in the y-z section between $\hat{y} = 0.125$ and 0.875) substantially decreases with increasing structural gradient from GNT-1 to GNT-4, which is also consistent with $|\overline{\Delta\varepsilon_z^{p,A-D}}|$ by experimental measurement. The discrepancy between modeling and experiment for GNT-1 may result from the linear variation of yield strength across the depth in the model, whereas there exist several hardness plateaus in the experimental GNT-1 sample (Fig. 1c).

Generally, plastic strain gradients are accommodated by generation of GNDs, leading to the extra strengthening effect in GNT Cu. Fig. 6 shows the evolution of the spatial distribution of plastic strain gradients

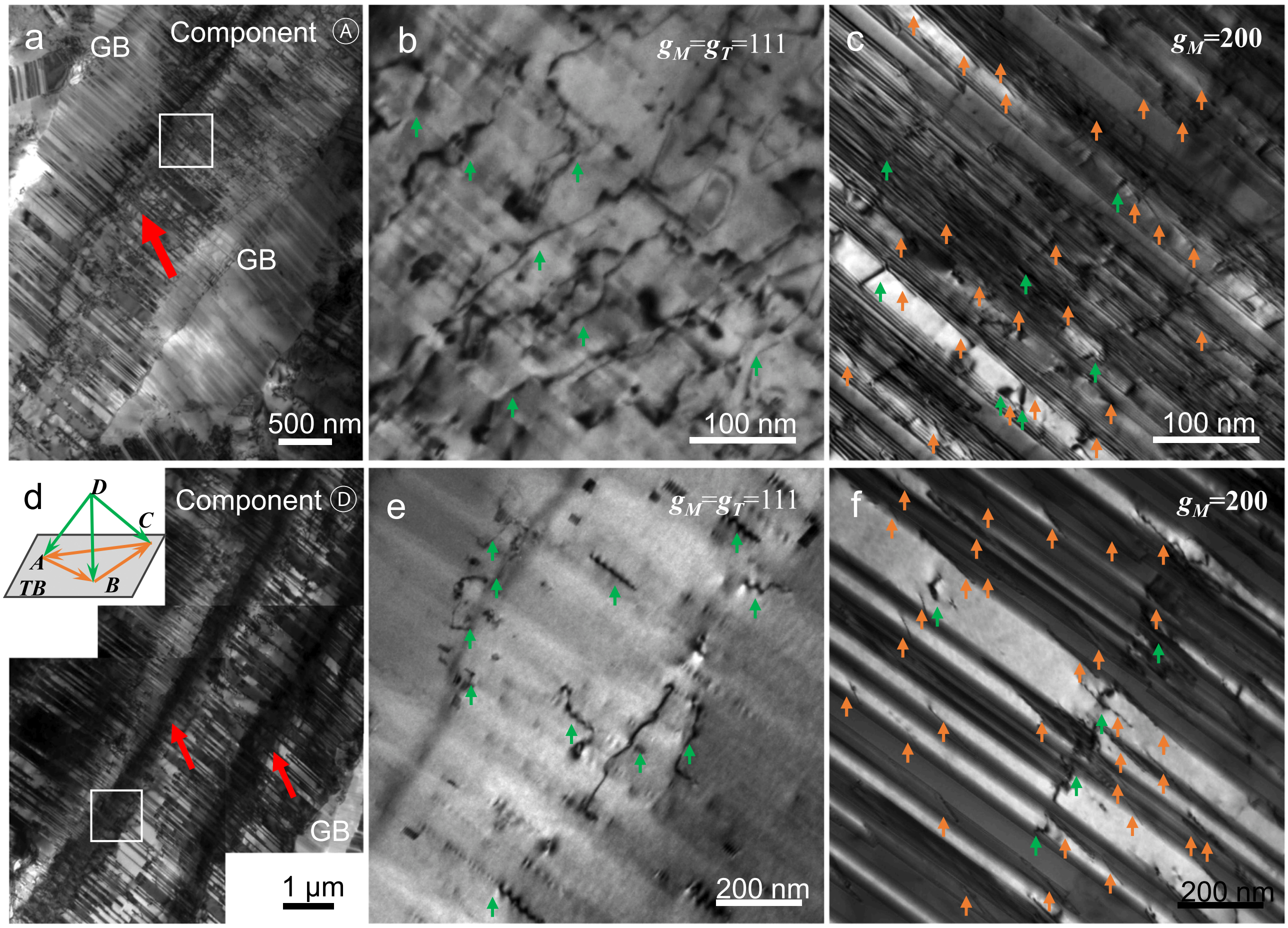

Fig. 4. TEM images of GNT-3 deformed at $\varepsilon = 1\%$. (a) Bundles of concentrated dislocations (BCD) are indicated by red arrow(s) in component Ⓐ (a) and component Ⓓ (d). Magnified TEM images (b, c) and (e, f) for the BCD in the white-box region in (a) and (d), respectively. (b, d) and (c, f) are imaged under diffraction vector of $g_M = g_T = 111$ and $g_M = 200$, respectively. Mode I and Mode II dislocations are indicated by green and orange arrows, respectively. GB, grain boundary. (For interpretation of the references to colour in this figure legend, the reader is referred to the web version of this article.)

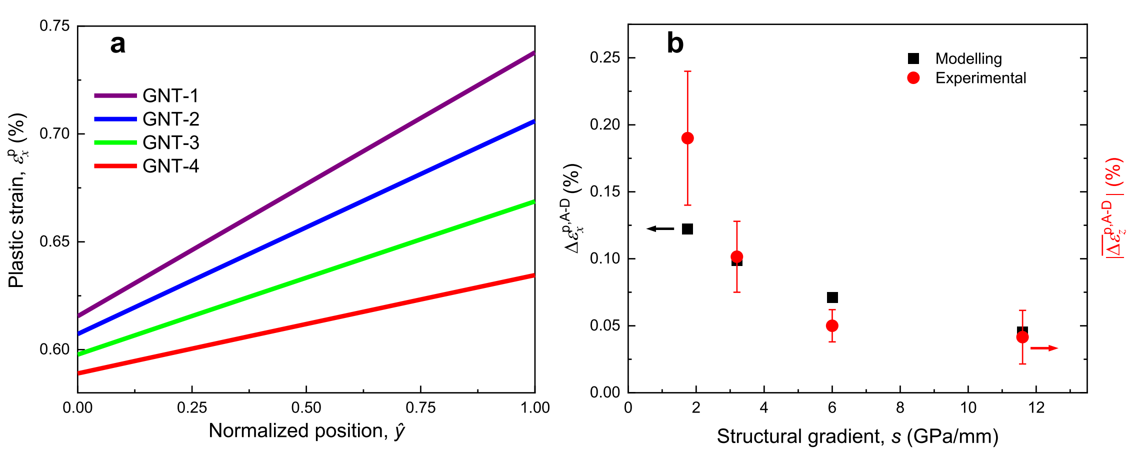

Fig. 5. SGP modeling results of plastic strains. (a) Distributions of plastic strains in the tensile direction for GNT-1 to GNT-4 at $\varepsilon = 1\%$. (b) $\Delta\varepsilon_x^{p,A-D}$ at $\varepsilon = 1\%$ against structural gradient from modeling predictions (black squares, left y axis) in comparison with $|\overline{\Delta\varepsilon_z^{p,A-D}}|$ from the experimental data (red circles, right y axis). (For interpretation of the references to colour in this figure legend, the reader is referred to the web version of this article.)

from numerical simulations of the 1D SGP model. For GNT-1, the region with non-zero plastic strain gradient $\nabla\varepsilon_x^{\mathbf{p}}$ first appears near $\hat{y}= 1$ in the initial stage of plastic deformation ($\varepsilon \leq 0.2\%$) and then expands to $\hat{y}= 0$ as the applied load increases (Fig. 6a). Such progressive yielding from $\hat{y}= 1$ to 0 corresponds to stage I in the local stress-strain curve in Ⓐ and Ⓓ, as shown in the inset of Fig. 6a. At the end of stage I ($\varepsilon = 0.4\%$), $\nabla\varepsilon_x^{\mathbf{p}}$ and the difference in the flow stress $\Delta\sigma^{A-D}$ (indicated by a double-headed arrow in the inset of Fig. 6a) reach the maximum. Thereafter, all Ⓐ to Ⓓ components undergo plastic deformation. Since the work hardening rate of Ⓓ is larger than that of Ⓐ, both $\Delta\sigma^{A-D}$ and $\nabla\varepsilon_x^{\mathbf{p}}$ drops a

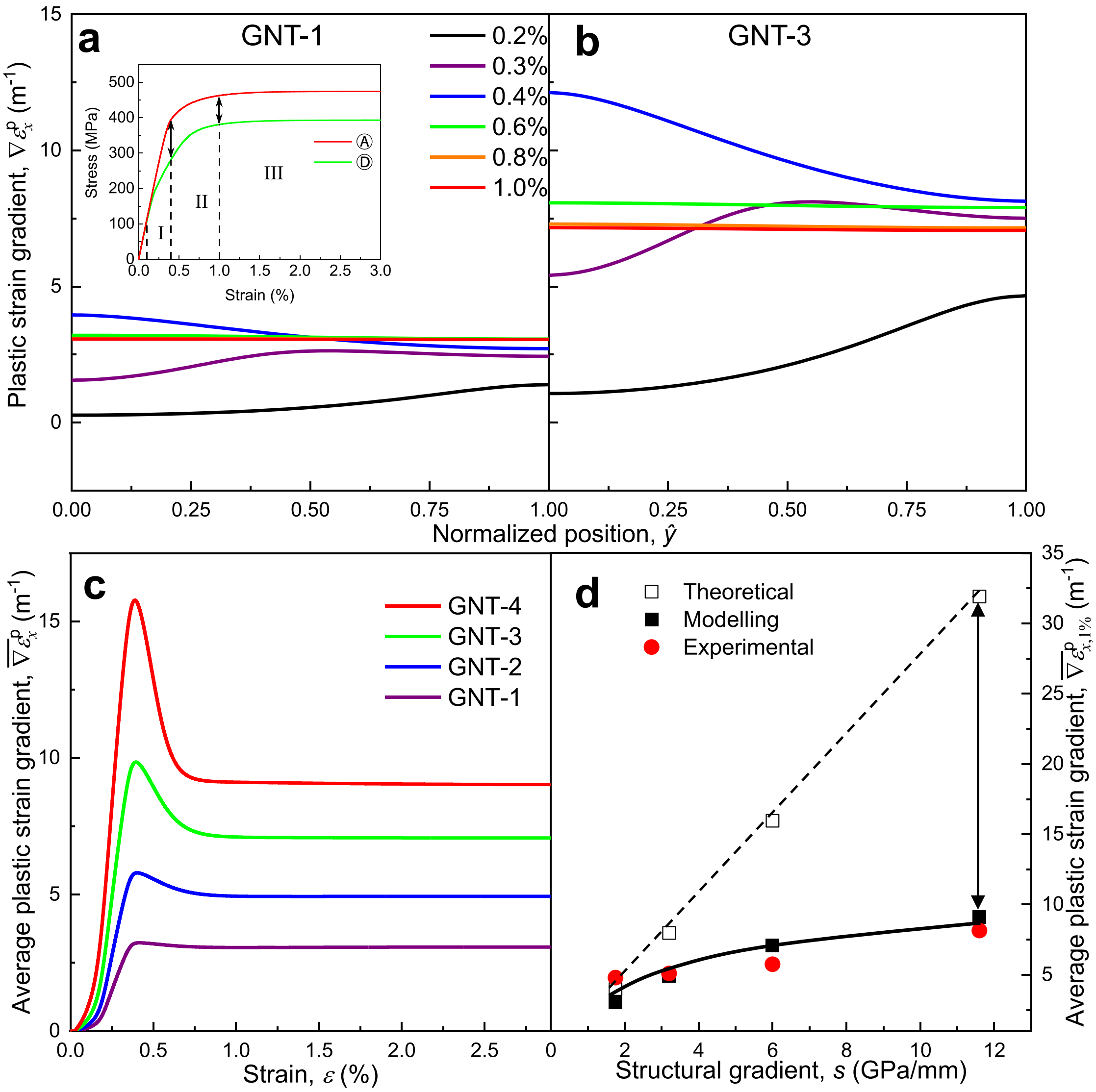

Fig. 6. SGP modeling results of plastic strain gradients. (a) Distribution of plastic strain gradient $\nabla\varepsilon_x^p$ in the *y-z* section of GNT-1 at different applied tensile strains. The inset shows the local tensile stress-strain curves of HNT-Ⓐ and Ⓓ. (b) Same as (a) except for GNT-3 (c) Evolution of the average plastic strain gradient across Ⓐ to Ⓓ components $\overline{\nabla\varepsilon_x^p}$ versus applied tensile strain for GNT-1 to GNT-4. (d) Comparison of $\overline{\nabla\varepsilon_x^p}$ at $\varepsilon = 1\%$ among the theoretical, modeling and experimental values versus structural gradient.

little. This deformation process corresponds to stage II in the inset of Fig. 6a. Beyond $\varepsilon = 1.0\%$ (stage III), the local stress-strain curves in Ⓐ and Ⓓ remain flat due to their almost saturated work hardening capability, and both $\nabla\varepsilon_x^p$ and $\Delta\sigma^{A-D}$ attain the respective saturated value. The saturated values of $\nabla\varepsilon_x^p$ at $\varepsilon = 1.0\%$ are almost the same (3.1 m^{-1}) across all Ⓐ to Ⓓ components.

Compared to GNT-1, GNT-3 exhibits a similar evolution of the spatial distribution of plastic strain gradients as shown in Fig. 6b. However, the saturated plastic strain gradient of GNT-3 (red curve) becomes larger ~7.1 m^{-1}, more than twice that of GNT-1. Furthermore, we calculated the average of plastic strain gradients $\overline{\nabla\varepsilon_x^p}$ over $\hat{y}$ for each GNT type. Fig. 6c shows the evolution of $\overline{\nabla\varepsilon_x^p}$ versus applied tensile strain ε. For each GNT type, $\overline{\nabla\varepsilon_x^p}$ first increases rapidly to a peak at $\varepsilon \sim 0.4\%$, then decreases to a saturated value at $\varepsilon \sim 1.0\%$ and beyond. The three stages of variation of $\overline{\nabla\varepsilon_x^p}$ correspond to the three stages in the local stress-strain curves in Ⓐ to Ⓓ components similar to those in the inset of Fig. 6a–d, both the SGP modeling and experimental results show that $\overline{\nabla\varepsilon_x^p}$ at $\varepsilon = 1.0\%$ increases with increasing structural gradient. Here, a theoretical estimate of the average plastic strain gradient $\overline{\nabla\varepsilon_{ref}^p}$ without considering the strengthening effect of structural gradient is roughly given as

$$\overline{\nabla\varepsilon_{ref}^p} \approx \frac{\Delta\sigma_Y^{A-D}}{El} \tag{7}$$

where $\Delta\sigma_Y^{A-D}$ represents the discrepancy in yield strength between freestanding HNT Ⓐ and Ⓓ components, l is the distance between component Ⓐ and Ⓓ and linearly decreases from ~400 to ~50 μm for GNT-1 to GNT-4, resulting in a marked increase of $\overline{\nabla\varepsilon_{ref}^p}$ as shown in Fig. 6d. It can be also seen that $\overline{\nabla\varepsilon_x^p}$ at $\varepsilon = 1.0\%$ in GNT-1 is comparable for the theoretical, modeling and experimental values, but a notable gap arises in GNT-2 and it becomes larger as the structural gradient increases. The deviation of $\overline{\nabla\varepsilon_x^p}$ corresponds to the reduced $|\overline{\Delta\varepsilon_z^{p,A-D}}|$ (Figs. 3 and 5b), both of which are related to the spatial distribution of local extra back stresses, as to be further discussed.

For GNT Cu under an applied tensile strain, its components Ⓐ to Ⓓ exhibit different ε_x^p and ε_z^p due to their different local yield strengths.

Specifically, component Ⓐ with the highest yield strength has the smallest magnitude of ε_x^p or ε_z^p. In contrast, component Ⓓ with the lowest yield strength has the largest magnitude of ε_x^p or ε_z^p. In other words, ε_z^p increases substantially from Ⓐ to Ⓓ, showing a gradient distribution of plastic strains (Figs. 1g and 2f). As a result, $\Delta\varepsilon_z^{p,A-D}$ can be estimated by

$$\Delta\varepsilon_z^{\mathbf{p,A-D}} = -\Delta\varepsilon_x^{\mathbf{p,A-D}} = -\frac{\Delta\sigma^{\mathbf{A-D}}}{E} \tag{8}$$

where $\Delta\sigma^{A-D}$ is the difference in flow stress at the same tensile strain between Ⓐ and Ⓓ; E is the elastic modulus. The plastic strain difference $\Delta\varepsilon_x^{p,A-D}$ is the same as the elastic strain difference (despite opposite signs) due to the same tensile strain for both Ⓐ and Ⓓ. By plugging the yield strengths of Ⓐ and Ⓓ [29] in Eq. (8), $\Delta\varepsilon_z^{p,A-D}$ is estimated as 0.19%, which is the same as the measured $|\overline{\Delta\varepsilon_z^{p,A-D}}|$ of GNT-1. This result indicates that the measured lateral strain $|\overline{\Delta\varepsilon_z^{p,A-D}}|$ in Fig. 3 can reflect the difference in the yield strength or flow stress between components Ⓐ and Ⓓ of GNT Cu samples. More importantly, the experimental results of gradient plastic strains can be used to improve the SGP theory to reveal the spatial inhomogeneous deformation of GNT Cu, which was not captured in the original and extended SGP theories [35,36]. Therefore, we improve the SGP theory by incorporating the grain size dependence of the saturated local extra back stress, so as to capture the distributions of plastic strains, plastic strain gradients and resultant local extra back stresses in GNT Cu.

3.4. Gradient distributions of extra back stresses from SGP modeling

In addition to the gradient distributions of plastic strains in (Section 3.3), the SGP modeling results reveal the gradient distributions of local extra back stresses and local extra strengths in GNT-1 to GNT-4. Similarly, we use GNT-1 and GNT-3 as examples for comparison. Fig. 7a–d show the distributions of local extra back stresses and local tensile stress in the y-z section of GNT-1 and GNT-3. In Fig. 7a, the local extra back stress increases from $\hat{y}$= 0 to 1 at different applied tensile strains in GNT-1. Similar to the evolution of the distribution of plastic strain gradients (Fig. 6a), the region with the non-zero local extra back stress gradually extends from $\hat{y}$= 1 to 0 during the progressive yielding process. It is worth noting that the local extra back stresses show a weak non-linear distribution as a result of progressive saturation of $\sigma_b^{GNT}(y)$ at small strains, approach an almost linear distribution toward the end of progressive yielding (ε = 0.4%), and finally attain a saturated linear distribution at ε = 1.0%. According to Eq. (5), the extra back stresses are proportional to the density of GNDs (i.e., plastic strain gradient) and grain size. The linear distribution of local extra back stresses results from the almost linear distribution of grain size which increases from $\hat{y}$= 0 to 1, i.e., from Ⓐ to Ⓓ (Fig. S1), since the saturated plastic strain gradient and the resultant GND density keep constant in the cross section (Fig. 6a).

The local extra strength is almost entirely determined by the local extra back stress. Fig. 7b shows the distribution of local tensile stresses $\sigma_{1\%}$ (red solid line) at the applied tensile strain ε = 1% in GNT-1. The HNT-induced local stress (black dashed line) is the sum of the local back stress and effective stress arising from uniform nanotwins [36], and it

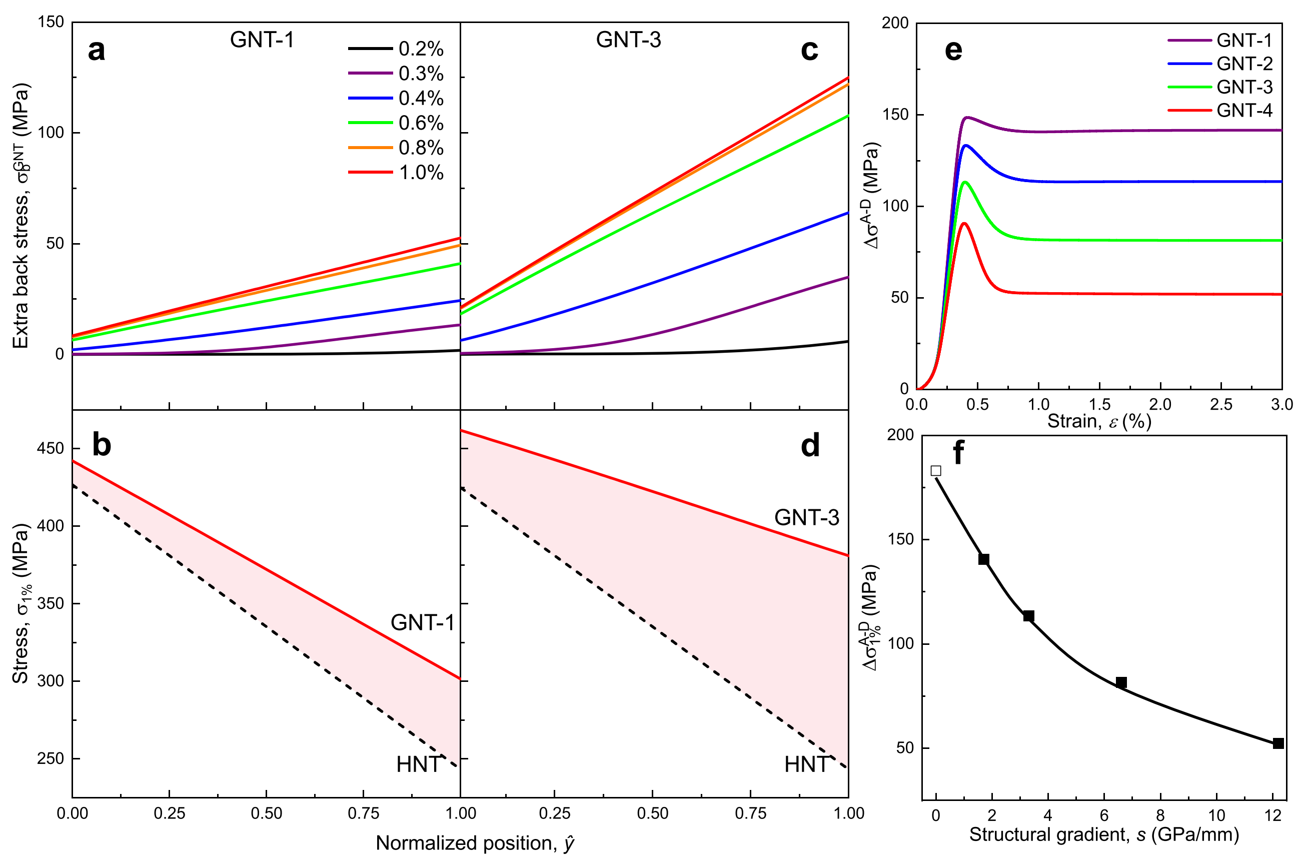

Fig. 7. SGP modeling results of local extra back stresses and flow stresses. (a) Distribution of local extra back stresses in the y-z section of GNT-1 at different applied tensile strains. (b) Corresponding distribution of local tensile stresses at ε = 1%. The red-shaded region between the local tensile stress (red solid line) and the HNT-induced local tensile stress (black dashed line) represents the extra strength. (c) Same as (a) except for GNT-3. (d) Same as (b) except for GNT-3. (e) The difference in local tensile stress between Ⓐ and Ⓓ $\Delta\sigma^{A-D}$ versus applied tensile strain for GNT-1 to GNT-4. (f) $\Delta\sigma^{A-D}$ at ε = 1% versus structural gradient. The open symbol represents the difference in stress between freestanding HNT Ⓐ and Ⓓ. (For interpretation of the references to colour in this figure legend, the reader is referred to the web version of this article.)

decreases linearly from $\hat{y}$= 0 to 1 (Ⓐ to Ⓓ). It is seen that $\sigma_{1\%}$ in GNT-1 is higher than the HNT-induced local stress due to the local extra strengthening effect. The saturated local extra strength at ε = 1% (indicated by the red shaded region) is almost the same as the local extra back stress as shown in Fig. 7a and accordingly becomes larger from $\hat{y}$= 0 to 1.

Compared to GNT-1, GNT-3 exhibits a similar distribution of local extra back stresses (Fig. 7c) and local tensile stresses (Fig. 7d). This is also verified by the distribution of hardnesses in deformed GNT-3 showing the increased hardening effect from Ⓐ to Ⓓ (Fig. S3). However, at a given $\hat{y}$, the saturated local extra back stress at $\varepsilon = 1\%$ is much higher in GNT-3 relative to GNT-1, and the increase in the local extra back stress is also much larger in Ⓓ than that in Ⓐ. As a result, a larger extra strengthening effect is found in GNT-3 and the saturated local extra strength at $\varepsilon = 1\%$ also becomes larger from $\hat{y}$= 0 to 1.

Fig. 7e shows that the difference in the tensile stress $\Delta\sigma^{A-D}$ (at $\hat{y}$= 0.125 and 0.875) first increases to a peak at $\varepsilon = 0.4\%$ and then decreases to a plateau at $\varepsilon = 1.0\%$ and beyond for all GNT Cu samples, which are consistent with the three deformation stages as shown in the inset of Fig. 6a. From GNT-1 to GNT-4, $\Delta\sigma^{A-D}$ markedly decreases due to the increasing local extra back stress and accordingly local extra strength especially in Ⓓ relative to Ⓐ (Figs. 7a–d and S2b). More specifically, $\Delta\sigma^{A-D}$ at ε = 1.0% decreases from 183 MPa for HNT Cu without structural gradient to 52 MPa for GNT-4 with the largest structural gradient (Fig. 7f), which is consistent with the prominent reduction of $|\overline{\Delta\varepsilon_z^{p,A-D}}|$ (Figs. 3 and 5b).

The combined experimental and SGP modeling results in this work reveal the spatial-temporal evolution of the strengthening effects arising from plastic strain gradients in GNT Cu, highlighting the gradient distributions of plastic strains, extra back stresses and extra strengths. Particularly, we note that according to the classical SGP theory or experiments [9,17], the strengthening effect of GNS metals is controlled by the plastic strain gradient and associated GND density, such that a higher GND density leads to a higher back stress and thus a stronger strengthening effect. In this work, we find that the uniform distributions of plastic strain gradients and accordingly GND densities in each type of GNT Cu can give rise to different local extra back stresses and thus local extra strengths. Our results suggest that the microstructure size itself such as the grain size (along with its gradient effect) can directly affect the local extra back stresses and thus local extra strengths, giving rise to the overall extra strength of GNT Cu. As a result, the gradient distribution of grain sizes in each type of GNT Cu yields the increased extra back stress from components Ⓐ to Ⓓ, which reduces the difference in the tensile flow stress and plastic strain across the components. This also suggests that the plastic deformation incompatibility of GNT Cu can be reduced due to the gradient distribution of local extra strengths. The underlying mechanism could be related to the increased amount of BCDs and associated GNDs with increased grain size from Ⓐ to Ⓓ. Hence, increasing the grain size while maintaining the same twin size gradient might be an effective strategy for further tuning the strength-ductility combination in GNT Cu. Furthermore, the gradient distribution of extra back stresses suggests that the strengthening effect of structural gradients may also be further enhanced by a moderate increase in the volume fraction of the soft components.

Finally, we point out that the gradient nanotwinned structure with a high density of stable low-energy TBs has the advantage of revealing the gradient plastic strain response to structural gradients, compared to the gradient nanograined structure with a high density of high-angle grain boundaries [49]. The nanograined surface layer in gradient nanograined materials usually exhibits unstable plastic deformation or softening via grain growth or shear banding [50], leading to increased plastic strains in hard components and thus decreased gradient strengthening effects. In contrast, the surface layer of GNT Cu contains more stable nanotwins, thereby promoting the sustained plastic deformation gradients from soft to hard components and thus an increased gradient strengthening effect.

4. Conclusion

Our combined experimental and SGP modeling results reveal the spatial-temporal evolution of local plastic strains, extra back stresses and extra strengths in GNT Cu. We find that the increased structural gradient reduces the maximum lateral strain difference between the hardest and softest components from full-field strain mapping. As a result, the softer component with a lower initial yield strength gains more extra strengths than the harder one, and such gain is amplified with an increase in structural gradient. The SGP modeling results indicate that the local extra back stress depends not only on the plastic strain gradient and associated GND density but also on the grain size. A larger grain size gives rise to a higher local extra back stress and thus a higher local extra strength, leading to the reduced difference in plastic strain between the hardest and softest components. These findings highlight the importance of quantifying the spatial-temporal evolution of plastic strain distributions by full-field strain mapping for elucidating both the local and overall strengthening effects of GNT Cu. Broadly, this work provides an in-depth mechanistic understanding of the strengthening effects of gradient microstructures toward a rational development of high-performance gradient nanostructured metals in the future.

Declaration of Competing Interest

The authors declare that they have no known competing financial interests or personal relationships that could have appeared to influence the work reported in this paper

Acknowledgments

L. acknowledges financial support from the National Natural Science Foundation of China (NSFC, Grant Nos 51931010, 92163202), and the Key Research Program of Frontier Science and International Partnership Program (GJHZ2029), Z.C. acknowledges financial support from National Natural Science Foundation of China (NSFC, Grant No. 52001312), China Postdoctoral Science Foundation (Grant Nos. BX20190336 and 2019M661150) and the IMR Innovation Fund (Grant No. 2021-PY02).

Supplementary materials

Supplementary material associated with this article can be found, in the online version, at doi:10.1016/j.actamat.2023.118673.

References

[1] T.H. Fang, W.L. Li, N.R. Tao, K. Lu, Revealing extraordinary intrinsic tensile plasticity in gradient nano-grained copper, Science 331 (6024) (2011) 1587–1590.
[2] X. Wu, M. Yang, F. Yuan, G. Wu, Y. Wei, X. Huang, Y. Zhu, Heterogeneous lamella structure unites ultrafine-grain strength with coarse-grain ductility, Proc. Natl. Acad. Sci. U. S. A. 112 (47) (2015) 14501–14505.
[3] E. Ma, T. Zhu, Towards strength–ductility synergy through the design of heterogeneous nanostructures in metals, Mater. Today 20 (6) (2017) 323–331.
[4] X. Li, L. Lu, J. Li, X. Zhang, H. Gao, Mechanical properties and deformation mechanisms of gradient nanostructured metals and alloys, Nat. Rev. Mater. 5 (9) (2020) 706–723.
[5] Y. Zhu, K. Ameyama, P.M. Anderson, I.J. Beyerlein, H. Gao, H.S. Kim, E. Lavernia, S. Mathaudhu, H. Mughrabi, R.O. Ritchie, N. Tsuji, X. Zhang, X. Wu, Heterostructured materials: superior properties from hetero-zone interaction, Mater. Res. Lett. 9 (1) (2021) 1–31.
[6] Z.Q. Liu, M.A. Meyers, Z.F. Zhang, R.O. Ritchie, Functional gradients and heterogeneities in biological materials: design principles, functions, and bioinspired applications, Prog. Mater. Sci. 88 (2017) 467–498.
[7] P. Sathiyamoorthi, H.S. Kim, High-entropy alloys with heterogeneous microstructure: processing and mechanical properties, Prog. Mater. Sci. 123 (2022), 100709.
[8] K. Lu, Making strong nanomaterials ductile with gradients, Science 345 (6203) (2014) 1455–1456.
[9] M.F. Ashby, The deformation of plastically non-homogeneous materials, Philos. Mag. 21 (170) (1970) 399–424.
[10] N. Fleck, G. Muller, M.F. Ashby, J.W. Hutchinson, Strain gradient plasticity: theory and experiment, Acta Metall. Mater. 42 (2) (1994) 475–487.

[11] M. Yang, Y. Pan, F. Yuan, Y. Zhu, X. Wu, Back stress strengthening and strain hardening in gradient structure, Mater. Res. Lett. 4 (3) (2016) 145–151.
[12] Y. Wei, Y. Li, L. Zhu, Y. Liu, X. Lei, G. Wang, Y. Wu, Z. Mi, J. Liu, H. Wang, H. Gao, Evading the strength-ductility trade-off dilemma in steel through gradient hierarchical nanotwins, Nat. Commun. 5 (2014) 3580.
[13] H. Wu, G. Fan, An overview of tailoring strain delocalization for strength-ductility synergy, Prog. Mater. Sci. 113 (2020) 100675.
[14] Y. Lin, J. Pan, H.F. Zhou, H.J. Gao, Y. Li, Mechanical properties and optimal grain size distribution profile of gradient grained nickel, Acta Mater. 153 (2018) 279–289.
[15] Z. Zeng, X. Li, D. Xu, L. Lu, H. Gao, T. Zhu, Gradient plasticity in gradient nano-grained metals, Extrem. Mech. Lett. 8 (2016) 213–219.
[16] J. Zhao, X. Lu, F. Yuan, Q. Kan, S. Qu, G. Kang, X. Zhang, Multiple mechanism based constitutive modeling of gradient nanograined material, Int. J. Plast. 125 (2020) 314–330.
[17] X. Wu, P. Jiang, L. Chen, F. Yuan, Y.T. Zhu, Extraordinary strain hardening by gradient structure, Proc. Natl. Acad. Sci. U. S. A. 111 (20) (2014) 7197–7201.
[18] J. Li, S. Chen, X. Wu, A.K. Soh, A physical model revealing strong strain hardening in nano-grained metals induced by grain size gradient structure, Mater. Sci. Eng. A 620 (2015) 16–21.
[19] Y.F. Wang, M.S. Wang, X.T. Fang, F.J. Guo, H.Q. Liu, R.O. Scattergood, C.X. Huang, Y.T. Zhu, Extra strengthening in a coarse/ultrafine grained laminate: role of gradient interfaces, Int. J. Plast. 123 (2019) 196–207.
[20] W.D. Nix, H. Gao, Indentation size effects in crystalline materials: a law for strain gradient plasticity, J. Mech. Phys. Solids 46 (3) (1998) 411–425.
[21] L.P. Kubin, A. Mortensen, Geometrically necessary dislocations and strain-gradient plasticity: a few critical issues, Scr. Mater. 48 (2) (2003) 119–125.
[22] K.E. Aifantis, W.A. Soer, J.T.M. De Hosson, J.R. Willis, Interfaces within strain gradient plasticity: theory and experiments, Acta Mater. 54 (19) (2006) 5077–5085.
[23] C.J. Bayley, W.A.M. Brekelmans, M.G.D. Geers, A comparison of dislocation induced back stress formulations in strain gradient crystal plasticity, Int. J. Solids Struct. 43 (24) (2006) 7268–7286.
[24] H. Mughrabi, On the current understanding of strain gradient plasticity, Mater. Sci. Eng. A 387 (2004) 209–213. -389.
[25] X. Wu, M. Yang, R. Li, P. Jiang, F. Yuan, Y. Wang, Y. Zhu, Y. Wei, Plastic accommodation during tensile deformation of gradient structure, Sci. China Mater. 64 (6) (2021) 1534–1544.
[26] X. Bian, F. Yuan, X. Wu, Y. Zhu, The evolution of strain gradient and anisotropy in gradient-structured metal, Metall. Mater. Trans. A 48 (9) (2017) 3951–3960.
[27] C.X. Huang, Y.F. Wang, X.L. Ma, S. Yin, H.W. Höppel, M. Göken, X.L. Wu, H.J. Gao, Y.T. Zhu, Interface affected zone for optimal strength and ductility in heterogeneous laminate, Mater. Today 21 (7) (2018) 713–719.
[28] M.N. Hasan, Y.F. Liu, X.H. An, J. Gu, M. Song, Y. Cao, Y.S. Li, Y.T. Zhu, X.Z. Liao, Simultaneously enhancing strength and ductility of a high-entropy alloy via gradient hierarchical microstructures, Int. J. Plast. 123 (2019) 178–195.
[29] Z. Cheng, H. Zhou, Q. Lu, H. Gao, L. Lu, Extra strengthening and work hardening in gradient nanotwinned metals, Science 362 (6414) (2018) eaau1925.
[30] Z. Cheng, L. Lu, The effect of gradient order on mechanical behaviors of gradient nanotwinned Cu, Scr. Mater. 164 (2019) 130–134.
[31] T. Wan, Z. Cheng, L. Bu, L. Lu, Work hardening discrepancy designing to strengthening gradient nanotwinned Cu, Scr. Mater. 201 (2021), 113975.
[32] Y. Wang, G. Yang, W. Wang, X. Wang, Q. Li, Y. Wei, Optimal stress and deformation partition in gradient materials for better strength and tensile ductility: a numerical investigation, Sci. Rep. 7 (1) (2017) 10954.
[33] J. Li, G.J. Weng, S. Chen, X. Wu, On strain hardening mechanism in gradient nanostructures, Int. J. Plast. 88 (2017) 89–107.
[34] X. Lu, J. Zhao, Z. Wang, B. Gan, J. Zhao, G. Kang, X. Zhang, Crystal plasticity finite element analysis of gradient nanostructured TWIP steel, Int. J. Plast. 130 (2020) 102703.
[35] Y. Zhang, Z. Cheng, L. Lu, T. Zhu, Strain gradient plasticity in gradient structured metals, J. Mech. Phys. Solids 140 (2020), 103946.
[36] Z. Cheng, L. Bu, Y. Zhang, H. Wu, T. Zhu, H. Gao, L. Lu, Unraveling the origin of extra strengthening in gradient nanotwinned metals, Proc. Natl. Acad. Sci. U. S. A. 119 (3) (2022), e2116808119.
[37] H. Mughrabi, A two-parameter description of heterogeneous dislocation distributions in deformed metal crystals, Mater. Sci. Eng. 85 (1987) 15–31.
[38] D. Kuhlmann-Wilsdorf, Theory of plastic deformation:-properties of low energy dislocation structures, Mater. Sci. Eng. A 113 (1989) 1–41.
[39] D. Kuhlmann-Wilsdorf, C. Laird, Dislocation behavior in fatigue II. friction stress and back stress as inferred from an analysis of hysteresis loops, Mater. Sci. Eng. 37 (2) (1979) 111–120.
[40] C.W. Sinclair, W.J. Poole, Y. Bréchet, A model for the grain size dependent work hardening of copper, Scr. Mater. 55 (8) (2006) 739–742.
[41] C.W. Bert, E.J. Mills, W.S. Hyler, Effect of variation in Poisson's ratio on plastic tensile instability, J. Basic Eng. 89 (1) (1967) 35–39.
[42] Z.S. You, L. Lu, K. Lu, Tensile behavior of columnar grained Cu with preferentially oriented nanoscale twins, Acta Mater. 59 (18) (2011) 6927–6937.
[43] Q. Pan, H. Zhou, Q. Lu, H. Gao, L. Lu, History-independent cyclic response of nanotwinned metals, Nature 551 (7679) (2017) 214–217.
[44] Z. You, X. Li, L. Gui, Q. Lu, T. Zhu, H. Gao, L. Lu, Plastic anisotropy and associated deformation mechanisms in nanotwinned metals, Acta Mater. 61 (1) (2013) 217–227.
[45] D. Viladot, M. VÉRon, M. Gemmi, F. PeirÓ, J. Portillo, S. EstradÉ, J. Mendoza, N. Llorca-Isern, S. Nicolopoulos, Orientation and phase mapping in the transmission electron microscope using precession-assisted diffraction spot recognition: state-of-the-art results, J. Microsc. 252 (1) (2013) 23–34.
[46] X. Ma, C. Huang, J. Moering, M. Ruppert, H.W. Höppel, M. Göken, J. Narayan, Y. Zhu, Mechanical properties of copper/bronze laminates: Role of interfaces, Acta Mater. 116 (2016) 43–52.
[47] Q. Lu, Z. You, X. Huang, N. Hansen, L. Lu, Dependence of dislocation structure on orientation and slip systems in highly oriented nanotwinned Cu, Acta Mater. 127 (2017) 85–97.
[48] H. Gao, Y. Huang, Geometrically necessary dislocation and size-dependent plasticity, Scr. Mater. 48 (2) (2003) 113–118.
[49] K. Lu, Stabilizing nanostructures in metals using grain and twin boundary architectures, Nat. Rev. Mater. 1 (5) (2016).
[50] T.H. Fang, N.R. Tao, K. Lu, Tension-induced softening and hardening in gradient nanograined surface layer in copper, Scr. Mater. 77 (2014) 17–20.